SCIENCE ADVANCES | RESEARCH ARTICLE

OPTICS

Ultrawide-bandwidth high-resolution all-optical intravascular ultrasound using miniaturized photoacoustic transducer

Lei Wang[1], Yongwen Zhao[1], Bo Zheng[2], Yong Huo[2], Yubo Fan[1]*, Dinglong Ma[1]*, Ying Gu[3]*, Pu Wang[1]*

Conventional intravascular ultrasound (IVUS) uses piezoelectric transducers to electrically generate and receive ultrasound. However, it remains a challenge to achieve large bandwidth for high resolution without compromising imaging depth. We report an all-optical IVUS (AO-IVUS) imaging system using picosecond laser pulse–pumped carbon composite for ultrasound excitation and π-phase–shifted fiber Bragg gratings for ultrasound detection. Using this all-optical technique, we achieved ultrawide-bandwidth (147%) and high-resolution (18.6 micrometers) IVUS imaging, which is unattainable by conventional technique. Imaging performance has been characterized in phantoms, presenting 18.6-micrometer axial resolution, 124-micrometer lateral resolution, and 7-millimeter imaging depth. Rotational pullback imaging scans are performed in rabbit iliac artery, porcine coronary artery, and rabbit arteries with drug-eluting metal stents, in parallel with commercial intravenous ultrasound scans as reference. Results demonstrated the advantages of high-resolution AO-IVUS in delineating details in vascular structures, showing great potential in clinical applications.

INTRODUCTION

Cardiovascular disease has been the leading cause of disability and death globally over the past 20 years, accounting for 8.9 million deaths in 2019 (*1*). Intravascular ultrasound (IVUS) plays an active role in the assessment of cardiovascular disease and has been an essential instrument in the cardiac catheterization laboratory for more than 30 years (*2*–*4*). However, because of the limited bandwidth of conventional piezoelectric transducers (PZTs), which is approximately 40% of its center frequency and the high attenuation of high-frequency ultrasound in blood, IVUS must make tradeoff between image resolution and penetration depth (*3*, *5*, *6*). Dual-modality intravascular imaging system combining IVUS with optical coherence tomography has been introduced to address the need for simultaneous high depth and high resolution (*7*, *8*). However, this solution poses its unique challenge in instrumentation (*8*, *9*), while inheriting some of the limitations, such as the clinical applicability for administering blood-clearing agents (*7*, *10*).

All-optical ultrasound techniques, which use light instead of electricity as the medium for ultrasound generation and detection, are emerging alternatives to the conventional piezoelectric-based ultrasound technique (*11*–*19*). All-optical IVUS (AO-IVUS) provides a promising solution for simultaneous high penetration depth and high imaging resolution. This is achieved through substantial improvement of frequency response bandwidth in both the excitation and detection of ultrasound using optical techniques. The past decade has seen great advances in both optical excitation of ultrasound (*20*–*27*) and optical detection of ultrasound (*28*–*36*), demonstrating a wide variety of technical solutions. Nevertheless, previous efforts on AO-IVUS have not fully exploited the potential of optical ultrasound excitation and detection, yielding limited ultrasound frequency response bandwidth and resolution. To date, AO-IVUS has yet to demonstrate high-resolution imaging with comparable image quality of current commercial IVUS system. To fully leverage the advantages of all-optical ultrasound techniques, proper selection of ultrasound generation and detection techniques and optimization of system and catheter design are required for an optimal solution of AO-IVUS (see table S3 and S4).

This study demonstrates an all-optical ultrasound imaging system with ultrawide bandwidth and a focused single-element transducer design specifically optimized for high-resolution intravascular imaging of blood vessels (Fig. 1A). Ultrawide-bandwidth ultrasound generation is realized through photoacoustic excitation of an ultrathin concave multiwall carbon nanotube and a polymethyl methacrylate (MWCNT-PMMA) composite using subnanosecond laser pulse. Meanwhile, ultrawide-bandwidth ultrasound detection is implemented using a π-phase–shifted fiber Bragg grating (π-FBG) sensor. We report the design and characterization of the AO-IVUS imaging system and a 3.9-Fr catheter with a center frequency of 27.5 MHz and a −6-dB bandwidth of 147% (Fig. 1B). This implementation of AO-IVUS results in 18.6-μm axial resolution and 124-μm lateral resolution. The imaging performance of the AO-IVUS system is verified by subresolution target phantom imaging and evaluated by two-dimensional (2D)/3D scans of rabbit illiac arteries, porcine coronary arteries, and rabbit arteries with drug-eluting metal stents (DES), demonstrating high-resolution imaging in ex vivo vasculature.

---

[1]Key Laboratory of Biomechanics and Mechanobiology (Beihang University), Ministry of Education, Institute of Medical Photonics, Beijing Advanced Innovation Center for Biomedical Engineering, School of Biological Science and Medical Engineering, Beihang University, Beijing 100191, China. [2]Institute of Cardiovascular Disease, Peking University First Hospital, Beijing 100034, China. [3]Department of Laser Medicine, The First Medical Center, Chinese PLA General Hospital, Beijing 100039, China.
*Corresponding author. Email: puwang@buaa.edu.cn (P.W.); guyinglaser301@163.com (Y.G.); dlmikema@buaa.edu.cn (D.M.); yubofan@buaa.edu.cn (Y.F.)

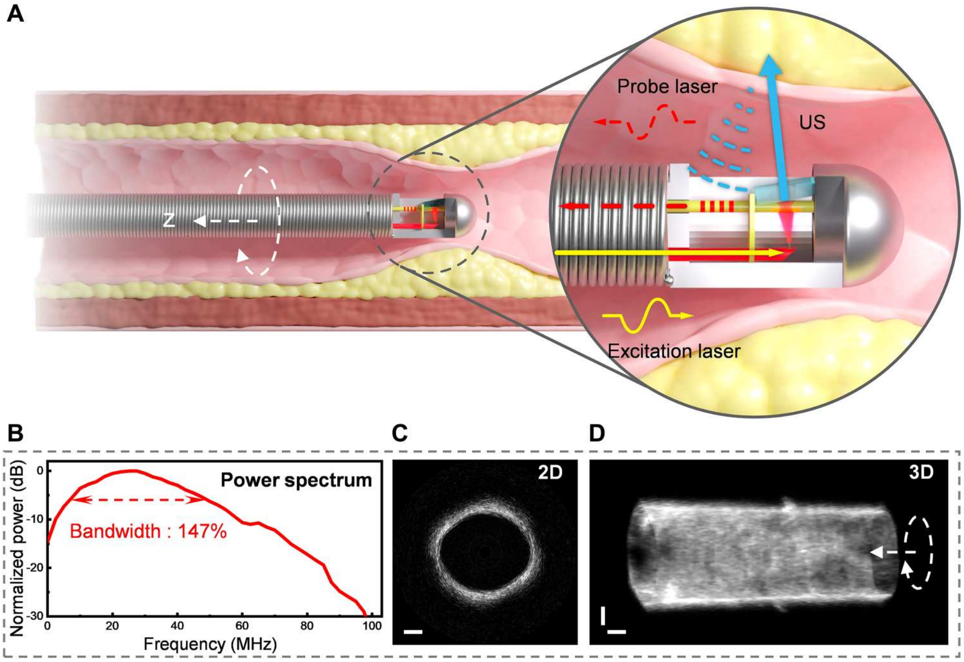

Fig. 1. Concept of ultrawide-bandwidth AO-IVUS. (**A**) Schematic of AO-IVUS imaging of vessel wall. (**B**) Power spectrum of AO-IVUS catheter ultrasound response. (**C**) Cross-sectional 2D image acquired by AO-IVUS. (**D**) 3D ultrasound data of arterial wall by rotational pullback scan of AO-IVUS. Scale bars, 1 mm.

RESULTS

AO-IVUS imaging system and catheter

The design and implementation of the AO-IVUS imaging system and catheter is illustrated in Fig. 2. Figure 2A shows a cross-sectional view of the AO-IVUS catheter. To generate a moderately focused ultrasound beam, a photoacoustic transducer is fabricated by forming an MWCNT-PMMA composite membrane with 5-μm thickness and 3-mm radius of curvature (Fig. 2B). The fabrication process of the MWCNT-PMMA photoacoustic transducer can be found in section S1. To generate ultrasound pressure wave, excitation laser pulse is delivered within the catheter via a multimode fiber side-polished at 42° illuminating on the photoacoustic transducer. Backscattered ultrasound from the vessel wall is collected by a π-FBG sensor (Yisan Optoelectronics Technology, Wuhan, China) for ultrasound detection. An accessory backing material is attached to the π-FBG section to absorb residual acoustic energy and alter the ultrasound frequency response of the fiber-optic π-FBG sensor. Details of this topic can be found in section S2. A tungsten ultrasound shielding plate is used to isolate the excitation elements from the detection elements. Last, the catheter is packaged by a round tip housing (1.3 mm by 2.4 mm, diameter by length) and a torque coil (1.3 mm by 100 cm, diameter by length), as demonstrated in Fig. 2 (C and D).

The setup of the AO-IVUS imaging system is shown in Fig. 2E. A microchip-pulsed laser (750-ps pulse width, 5-kHz repetition rate; MCG-1064-100-003, RealLight Technology, Beijing, China) is used for ultrasound excitation by beam coupling into a 50-μm core diameter multimode fiber with a distal end output pulse energy of 6 μJ. A narrow linewidth tunable laser (TLB-6728, New Focus, USA) with a wavelength tuning range from 1520 to 1570 nm and a linewidth of 200 kHz is used to interrogate the π-FBG using edge detection methods (*37*). The interrogating laser is coupled into the single mode fiber of the π-FBG and reflected by its grating resonance line, which is modulated by the ultrasound signal incident on the π-FBG grating section. The returning modulated optical signal is detected by a high-speed photodiode (1811-FS, New Focus, USA) with separate DC (<50 kHz) and AC (50 kHz to 125 MHz) output. The low-frequency signal accounts for π-FBG line shifts induced by mechanical vibration, strain, and temperature drifts; it is acquired by a 1.25 MSa/s data acquisition (DAQ) card in PC; a digital proportional-integral-derivative (PID) controller is implemented to regulate the wavelength of the tunable laser to track the 50% reflectance wavelength of the π-FBG resonance slope using the laser line. Thus, the baseline of the reflected optical signal can be stabilized before the ultrasound signal is excited. On the other hand, the high-frequency signal is mostly associated with ultrasound detected by the π-FBG sensor; it is acquired by a 500 MSa/s DAQ card in PC (M-4i.4451, Spectrum, Germany) for ultrasound data processing and image reconstruction.

To implement the rotational pullback of the AO-IVUS catheter, a motorized fiber-optic rotary joint and catheter translation stage is constructed. The fiber-optic rotary joint relays the photoacoustic transducer excitation laser pulse and π-FBG sensor interrogation laser beam from the static system on the proximal end to the rotating catheter tip on the distal end. A photograph of the AO-IVUS system on benchtop configuration can be found in section S3.

System characterization

The ultrasound imaging performance of the AO-IVUS system was characterized by simulation and experiments, as demonstrated in Fig. 3. The ultrasound pulse echo response of the AO-IVUS system was measured (see Materials and Methods), and the time-domain pressure waveform and the corresponding frequency-domain spectra are presented in Fig. 3A. A hydrophone (ONDA

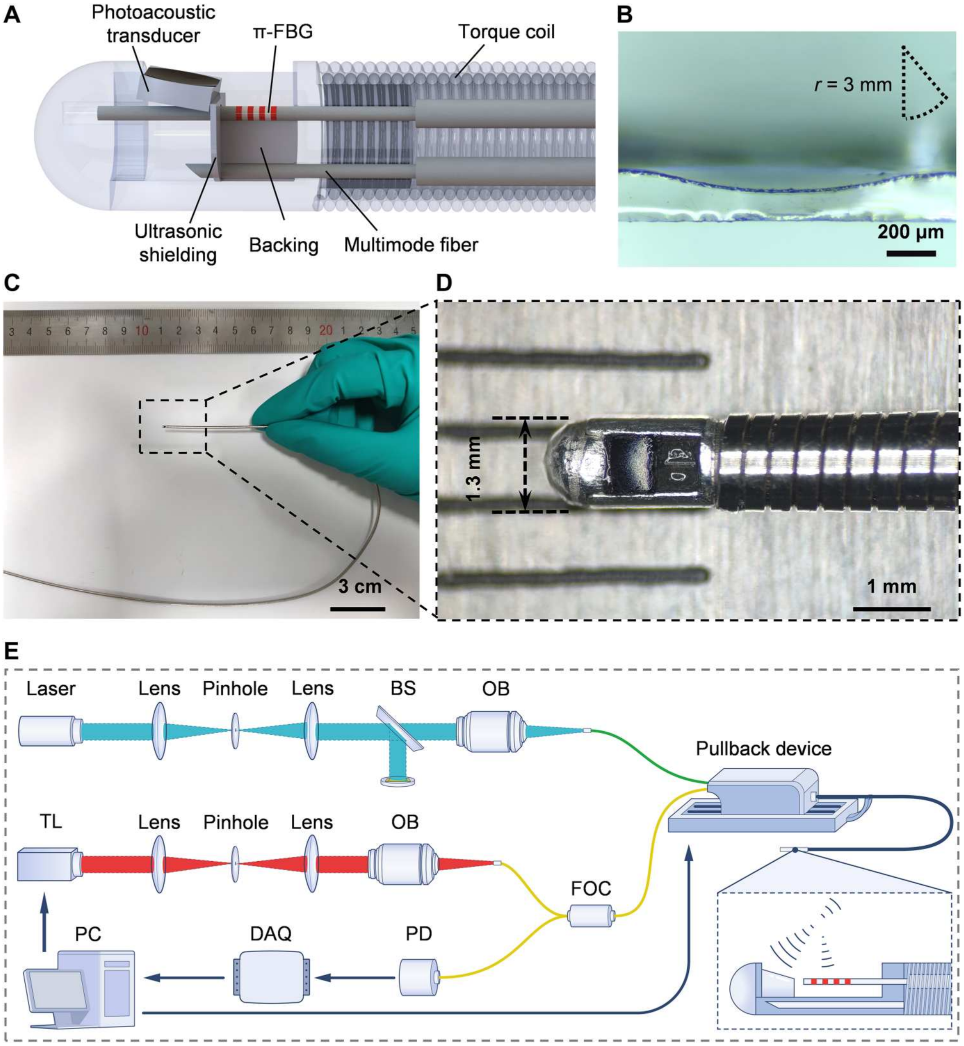

Fig. 2. AO-IVUS imaging system and catheter. (**A**) AO-IVUS catheter probe design. (**B**) Microscopic photo of concave photoacoustic transducer cross section. (**C**) Photograph of fabricated AO-IVUS catheter. (**D**) Close-up photograph of AO-IVUS catheter probe. (**E**) System configuration schematic of the AO-IVUS imaging system. BS, beam splitter; OB, objective; TL, tunable laser; FOC, fiber optical circulators; PC, personal computer; DAQ, data acquisition; PD, photodiode.

HGL-0085, ONDA, USA) was used to measure the pressure wave generated by the MWCNT-PMMA photoacoustic transducer, recording a 0.284-MPa pressure wave amplitude (peak-to-peak) and a −6-dB bandwidth of 52.7 MHz with a center frequency of 35.6 MHz. Subsequently, the π-FBG sensor in the AO-IVUS catheter was used to measure the pulse echo response, demonstrating a −6-dB bandwidth from 7.3 to 47.7 MHz, with a center frequency of 27.5 MHz. This corresponds to a fractional bandwidth of 147%, which suggests that a theoretical axial resolution of 18.6 μm can be achieved. A noise equivalent pressure (NEP) of 108 Pa is quantified on the basis of the SD of the noise baseline of the pulse echo waveform.

To evaluate the lateral resolution of the system, ultrasound field generated by the photoacoustic transducer was simulated using the k-wave toolbox in MATLAB, as demonstrated in Fig. 3B (*38*). Assuming an acoustic source with a circularly uniform field distribution at $z = 0$ distance, the acoustic field distribution profiles at 3 and 6 mm distance were simulated, presenting a lateral width [full width at half maximum (FWHM)] of 107 and 359 μm, respectively.

To evaluate the axial and lateral imaging resolution of the AO-IVUS system, a subresolution target phantom was scanned by the AO-IVUS catheter to acquire the imaging point spread function (PSF) of 12 helically arranged 10-μm diameter tungsten wires, as shown in Fig. 3C. The axial and lateral imaging resolution was quantified by fitting the cross-sectional profiles of the PSF to Gaussian function and taking the FWHM widths. The resulting axial and lateral resolution as functions of the target distance to the rotational center is presented in Fig. 3D. The optimal axial resolution of 22 μm and lateral resolution of 124 μm are found at 3.1-mm target distance, which is the closest target to the photoacoustic transducer focus (3 mm). The measured 22-μm width of the PSF is in accordance with the convoluted size between the 18.6-μm theoretical axial resolution and 10-μm diameter of the tungsten wire.

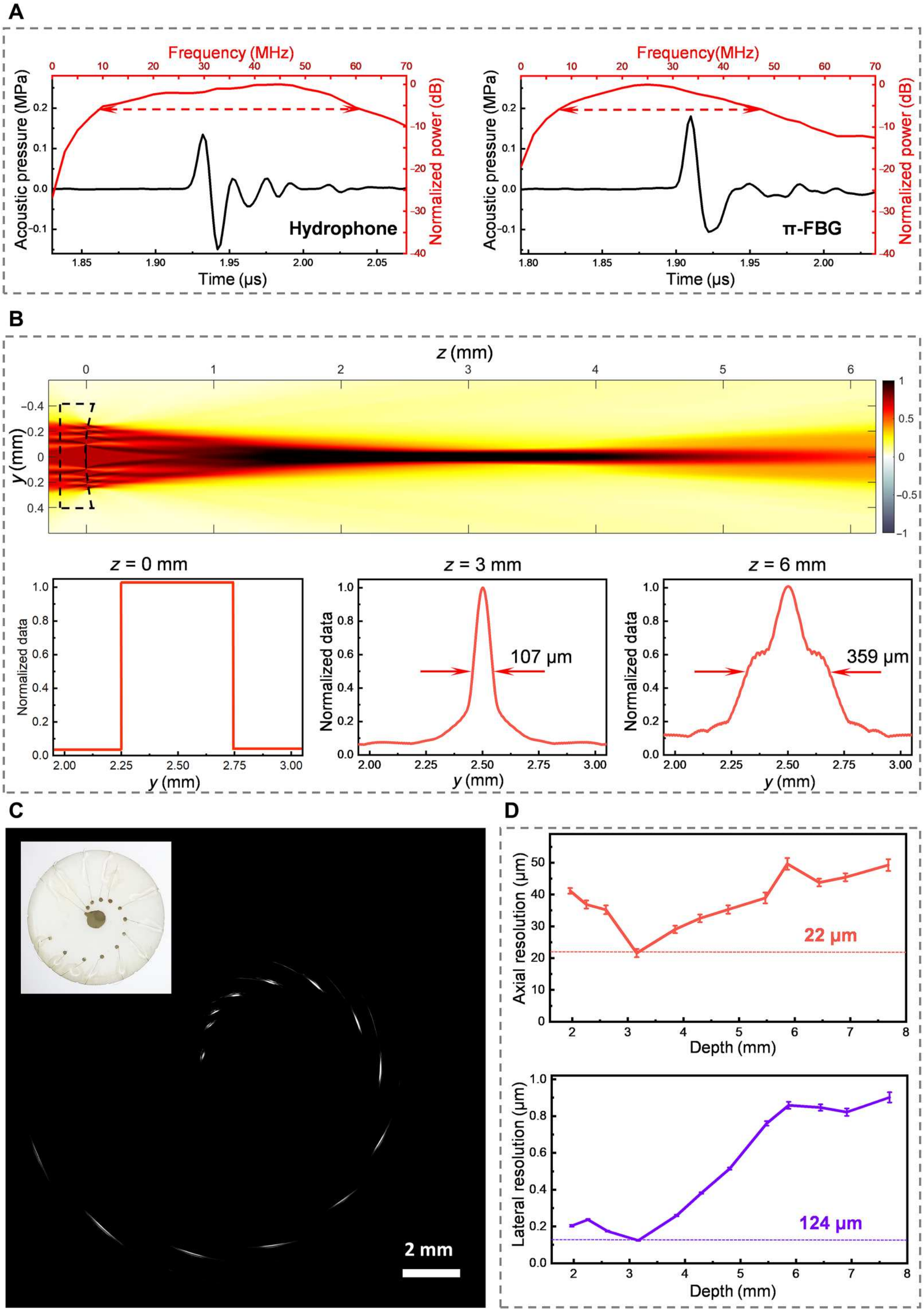

Fig. 3. AO-IVUS imaging system characterization. (**A**) Time-domain and frequency-domain ultrasound response of AO-IVUS measured by hydrophone (left) and π-FBG (right) in pulse echo mode. (**B**) Simulated ultrasound pressure field distribution in 2D. Uniform top-hat pressure wave distribution is assumed at the surface ($z = 0$) of the photoacoustic transducer, the ultrasound beam profiles at $z = 3$, and 6-mm distance result in 107- and 359-μm lateral width (FWHM). (**C**) Ultrasound B-scan image and photograph (top left inset) of a subresolution target phantom with 14 helically arranged 10-μm diameter tungsten wires. (**D**) Axial (top) and lateral (bottom) resolution of the AO-IVUS imaging system. The resolution values are quantified by the radial and tangential size of the tungsten wires in (C) at various distances from the catheter center.

Ex vivo vasculature imaging

To demonstrate the application of AO-IVUS in delineating vascular structures and other associated features such as stents, ex vivo vasculature imaging results are presented in Fig. 4. Ex vivo samples of rabbit iliac artery, porcine coronary artery, and rabbit artery with DES were assessed by the AO-IVUS system through rotational pullback imaging. A commercial 40-MHz IVUS catheter and imaging system (OptiCross and POLARIS, Boston Scientific, MA, USA) was adopted to acquire reference IVUS image data of the artery samples for comparison, as demonstrated in Fig. 4 (A and C). In Fig. 4 (A and B), the media and adventitia layers of healthy arterial tissue are both visible on the images AO-IVUS and commercial IVUS systems. In addition, a hypoechoic layer is clearly differentiated on the intima-media boundary in AO-IVUS images in Fig. 4B, which suggests that superior axial resolution of the AO-IVUS system might enable delineation of fine features on the vessel wall. In Fig. 4C, the stent struts of the DES are distinctively depicted on the AO-IVUS images, presenting a smaller circumferential length of 0.4 ± 0.1 mm at 2.0 ± 0.3 mm distance, compared to 1.1 ± 0.2 mm at 2.0 ± 0.5 mm distance in commercial IVUS images. In the commercial IVUS images of Fig. 4, the container bottom wall in which the samples were placed in saline bath is denoted by red arrows. Parts of adventitia and adipose tissue attached to the vessel wall can be observed in the IVUS images, but not in the AO-IVUS images, owing to tissue fixation and excision of detached tissue fragments. Further quantitative analysis of vessel morphology and stent structure can be found in section S5. Last, the applicability of AO-IVUS for 3D imaging of ex vivo vasculature is demonstrated in Fig. 4D (see also visualization 1). The stent structure of the DES is highlighted in 3D point cloud rendering based on AO-IVUS images, and the periodic pattern of the stent struts is parallel to the stent pattern revealed by the back-illuminated photograph.

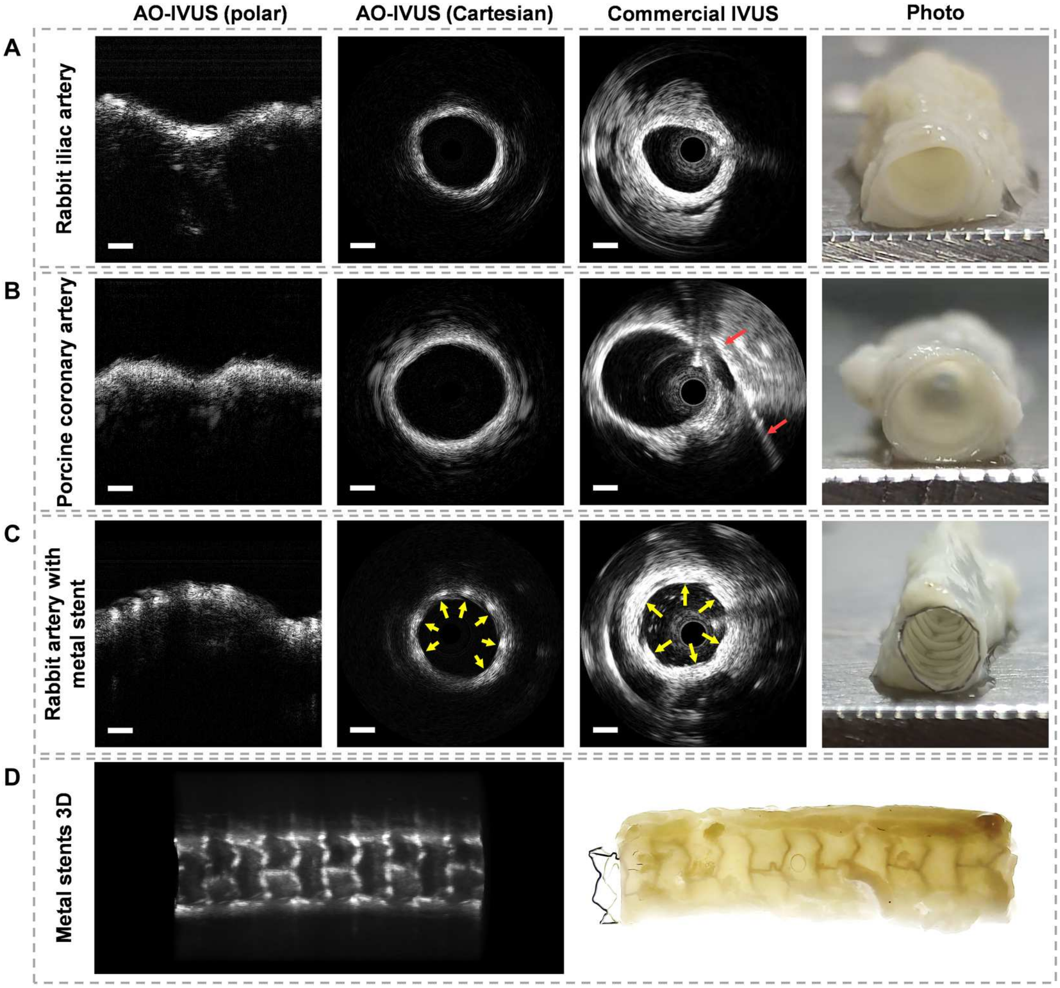

Fig. 4. Ex vivo vasculature imaging using AO-IVUS and commercial IVUS. (**A** to **C**) From left to right: AO-IVUS B-scan images in polar and Cartesian coordinates, conventional IVUS B-scan images, and photograph of the interrogated vessel samples. The ex vivo vasculature samples include (A) rabbit iliac artery, (B) porcine coronary artery, and (C) rabbit iliac artery with DES. The stent struts are demarcated by yellow arrows on AO-IVUS and commercial IVUS B-scan images [scale bars (all ultrasound images), 1 mm]. (**D**) (Left) 3D rendering based on AO-IVUS images of the DES structures in rabbit artery; (right) back-illuminated photograph of the rabbit artery sample with DES. Contrasts of both images were adjusted to highlight the stent features.

DISCUSSION

In this work, we demonstrated an ultrawide-bandwidth high-resolution ultrasound imaging technique that is optimized for IVUS imaging application. The combination of MWCNT-PMMA photoacoustic transducer and π-FBG sensor not only offers ultrawide-bandwidth frequency response of ultrasound excitation and detection but also enables compact form and ultrasound focusing.

For conventional IVUS using PZTs, the axial and lateral resolutions are both confined by the design (thickness, aperture size, etc.) and material characteristics of the PZT device. Inherent limitation of fractional bandwidth by the PZT material results in the unavoidable trade-off between penetration depth and imaging resolution. For commercial IVUS with a center frequency of 20 to 40 MHz, the typical axial resolution is around 80 μm, and lateral resolution is 200 to 250 μm (*39*). Higher bandwidth and better axial resolution are achievable by PZT-based IVUS through going to a higher center frequency, such as 60 MHz or even 100 MHz. On the other hand, all-optical techniques for ultrasound excitation and detection enable the possibilities to generate and receive ultrasound with a wider bandwidth without sacrificing low-frequency response and penetration depth.

MWCNT-PMMA material was chosen to implement the photoacoustic transducer, primarily because of its nice acoustic and optical properties (*40*, *41*) and the ease of fabrication and assembly. To optimize the ultrasound excitation bandwidth, excitation laser pulse duration (*42*–*44*), photoacoustic composite thickness (*45*), and material (*20*, *23*, *26*, *46*) are among the most important parameters to consider. Previous studies have shown that ultrasound bandwidth increases as the excitation laser pulse width or the photoacoustic composite thickness decreases, as shown in table S3. Therefore, subnanosecond laser pulse–excited ultrathin photoacoustic transducer in this work successfully demonstrated high-bandwidth ultrasound generation. Owing to the fabricability of MWCNT-PMMA material, the concave design of the transducer also facilitated the generation of the focused ultrasound beam and the improvement of the lateral imaging resolution.

For optical detection of ultrasound, sensors based on sensing acoustic perturbation of optical resonator mode are the most widely adopted solution for optical ultrasound detection (*47*, *48*), including the Fabry-Pérot interferometer for forward detection (*28*–*30*), a microring resonator for out-of-plane detection (*31*–*33*), and π-FBG for lateral detection (see table S4) (*34*–*36*). Since the π-FBG sensor is suitable for detecting laterally incident ultrasound, while fully compatible with the fiber-optic transcerving configuration of intravascular imaging, it is ideal for implementing AO-IVUS catheters. However, glass optical fiber exhibits characteristic ultrasound frequency response induced by resonances in the cross section, resulting in high responsivity at 30 and 80 MHz and low responsivity at 50 to 60 MHz (*49*). This discontinuity of ultrasound frequency response prevents the ultrasound detection bandwidth of the π-FBG sensor from being further improved (*36*, *50*). A technical optimization has been implemented by effectively altering the resonance modes of grating section of π-FBG by attaching an acoustic backing. It has demonstrated a notable enhancement in the ultrasound detection bandwidth of the π-FBG sensor. However, such design comes at a cost of reduction in high-frequency response. To achieve a higher center frequency while maintaining similar bandwidth, one possible solution is to use a fiber-optic waveguide with reduced cladding diameter to fabricate the π-FBG sensor.

Further improvements of intravascular imaging performance can be made in the following aspects: system, devices, and catheter design. The ultrasound detection NEP is currently limited by the phase noise of the narrow-line tunable laser (200 kHz linewidth). By adopting a π-FBG interrogation laser with 10- to 20-fold smaller linewidth, which is widely available commercially, the NEP can be reduced, and the SNR can be improved accordingly. Hence, the penetration depth can also be increased. In addition, alternative photoacoustic transducing materials that enable higher bandwidth and photoacoustic conversion efficiency, such as candle soot and polydimethylsiloxane, can be exploited to increase the bandwidth and pressure wave amplitude of the generated ultrasound and to potentially reduce the size of the catheter by reducing the surface area of the transducer that will withstand higher laser power density, although fabrication techniques of such materials that are compatible with catheter designs are yet to be developed. The lateral resolution can potentially be enhanced by inserting an acoustic lens on top of the receiving window of the AO-IVUS catheter. The limiting factor for the current AO-IVUS system to perform in vivo imaging is the wavelength tuning speed of the narrow-line laser for π-FBG interrogation, which is not fast enough to adjust the laser line per A-line at video rate imaging. By adopting high-speed tunable narrow-line laser, the wavelength adjustment frequency can be substantially increased to stabilize the detection baseline at real time.

In conclusion, we have demonstrated an ultrawide-bandwidth high-resolution AO-IVUS technique outperforming state-of-the-art commercial IVUS systems with 18.6-μm axial resolution and 124-μm lateral resolution. The design and implementation of the intravascular catheter and imaging system is characterized in phantoms and validated in ex vivo vasculatures, presenting clinical-grade, anatomically accurate images of vascular morphology and stent structures. This concept brings great potential to the clinical application of all-optical ultrasound techniques and future commercialization for the next-generation IVUS imaging technology.

MATERIALS AND METHODS

System characterization experiment

A 1064-nm laser with a pulse width of 0.75 μs was irradiated to the MWCNT-PMMA film (laser power density of 2.74 mJ/cm^2), and the calibrated hydrophone and π-FBG were used to detect the ultrasound on the opposite side to compare the response of the detection system. The time domain and frequency domain results of ultrasonic detection by hydrophone are shown in Fig. 3A. The time domain and frequency domain results of ultrasonic detection by π-FBG are shown in Fig. 3B.

Subresolution phantom construction and imaging

The AO-IVUS system was used to image tungsten filaments of 10 μm in diameter at various depths, and the results are shown in Fig. 3C. Among them, each A-line averages 50 times to improve the signal-to-noise ratio, and 2000 A-lines constitute an image. The data were processed by the Labview program, and the A-line data were processed by 5- to 130-MHz band-pass filter and then processed by synthetic aperture algorithm, taking envelope, logarithmic compression, and depth gain.

Ex vivo vessel preparation, commercial IVUS imaging, and sample fixation

This study was approved by an institutional review board, and all animal procedures were performed according to protocols approved by the Institutional Animal Care and Use Committee. The animal blood vessel samples used in this study were provided by Peking University First Hospital. The experimental rabbits were killed by humanitarian means, and their iliac artery vessels were obtained. Iliac artery vessels in rabbits were placed in saline and imaged using a commercial IVUS device (OptiCross, Boston Scientific, US). Meanwhile, the imaged iliac artery vessels were preserved in formalin solution.

Ex vivo vessel AO-IVUS imaging and data processing

The rabbit iliac artery vessels preserved in formalin solution were cleaned and placed in an AGAR mold and placed in a saline environment. The AO-IVUS system was used to perform 3D ring imaging of iliac artery vessels in rabbits. The imaging program is controlled by Labview software, and the data are stored in a PC. Each A-line averages 50 times to improve the signal-to-noise ratio. The A-line data are processed by filtering, taking envelope, logarithmic compression, and other algorithms, and 256 A-lines are used to get an image through coordinate transformation.

Resolution imaging and data processing

A tungsten wire with a diameter of 10 μm is passed through a specially made mold so that the tungsten wire is distributed at different depths from the center of the mold. These positions are 1 to 8 mm from the center of the mold and are used to characterize the resolution of the AO-IVUS system at different depths. 2D images of tungsten wires at different positions were performed using the AO-IVUS probe, and each image consisted of 2000 A-lines. Corresponding to the maximum point of each tungsten wire position in the original data, 200 points before and after the data were selected along the A-line for Gaussian fitting, and the FWHM after Gaussian fitting was used as the axial resolution data. At the same time, 200 points before and after the data are selected along the vertical A-line for Gaussian fitting, and the FWHM after Gaussian fitting is used as the lateral resolution data.

Supplementary Materials

This PDF file includes:

Supplementary Text
Figs. S1 to S6
Tables S1 to S4
References

View/request a protocol for this paper from *Bio-protocol*.

REFERENCES AND NOTES

1. G. A. Roth, G. A. Mensah, C. O. Johnson, G. Addolorato, E. Ammirati, L. M. Baddour, N. C. Barengo, A. Z. Beaton, E. J. Benjamin, C. P. Benziger, A. Bonny, M. Brauer, M. Brodmann, T. J. Cahill, J. Carapetis, A. L. Catapano, S. S. Chugh, L. T. Cooper, J. Coresh, M. Criqui, N. De Cleene, K. A. Eagle, S. Emmons-Bell, V. L. Feigin, J. Fernández-Solà, G. Fowkes, E. Gakidou, S. M. Grundy, F. J. He, G. Howard, F. Hu, L. Inker, G. Karthikeyan, N. Kassebaum, W. Koroshetz, C. Lavie, D. Lloyd-Jones, H. S. Lu, A. Mirijello, A. M. Temesgen, A. Mokdad, A. E. Moran, P. Muntner, J. Narula, B. Neal, M. Ntsekhe, G. M. de Oliveira, C. Otto, M. Owolabi, M. Pratt, S. Rajagopalan, M. Reitsma, A. L. P. Ribeiro, N. Rigotti, A. Rodgers, C. Sable, S. Shakil, K. Sliwa-Hahnle, B. Stark, J. Sundström, P. Timpel, I. M. Tleyjeh, M. Valgimigli, T. Vos, P. K. Whelton, M. Yacoub, L. Zuhlke, C. Murray, V. Fuster; GBD-NHLBI-JACC Global Burden of Cardiovascular Diseases Writing Group, Global burden of cardiovascular diseases and risk factors, 1990–2019: Update from the GBD 2019 study. *J. Am. Coll. Cardiol.* **76**, 2982–3021 (2020).
2. S. E. Nissen, P. Yock, Intravascular ultrasound. *Circulation* **103**, 604–616 (2001).
3. M. C. McDaniel, P. Eshtehardi, F. J. Sawaya, J. S. Douglas Jr, H. Samady, Contemporary clinical applications of coronary intravascular ultrasound. *JACC Cardiovasc. Interv.* **4**, 1155–1167 (2011).
4. H. M. Garcia-Garcia, M. A. Costa, P. W. Serruys, Imaging of coronary atherosclerosis: Intravascular ultrasound. *Eur. Heart J.* **31**, 2456–2469 (2010).
5. T. Ma, M. Yu, Z. Chen, C. Fei, K. K. Shung, Q. Zhou, Multi-frequency intravascular ultrasound (IVUS) imaging. *IEEE Trans. Ultrason. Ferroelectr. Freq. Control* **62**, 97–107 (2015).
6. C. E. Munding, E. Chérin, I. Jourard, J. J. Weyers, D. E. Goertz, B. K. Courtney, F. S. Foster, Development of a 3 french dual-frequency intravascular ultrasound catheter. *Ultrasound Med. Biol.* **44**, 251–266 (2018).
7. X. Li, J. Li, J. Jing, T. Ma, S. Liang, J. Zhang, D. Mohar, A. Raney, S. Mahon, M. Brenner, P. Patel, K. K. Shung, Q. Zhou, Z. Chen, Integrated IVUS-OCT imaging for atherosclerotic plaque characterization. *IEEE J. Sel. Top. Quantum Electron.* **20**, 7100108 (2014).
8. C. V. Bourantas, H. M. Garcia-Garcia, K. K. Naka, A. Sakellarios, L. Athanasiou, D. I. Fotiadis, L. K. Michalis, P. W. Serruys, Hybrid intravascular imaging. *J. Am. Coll. Cardiol.* **61**, 1369–1378 (2013).
9. X. Ma, W. Cao, Single-crystal high-frequency intravascular ultrasound transducer with 40-μm axial resolution. *IEEE Trans. Ultrason. Ferroelectr. Freq. Control* **67**, 810–816 (2019).
10. M. Ono, H. Kawashima, H. Hara, C. Gao, R. Wang, N. Kogame, K. Takahashi, P. Chichareon, R. Modolo, M. Tomaniak, J. J. Wykrzykowska, J. J. Piek, I. Mori, B. K. Courtney, W. Wijns, F. Sharif, C. Bourantas, Y. Onuma, P. W. Serruys, Advances in IVUS/OCT and future clinical perspective of novel hybrid catheter system in coronary imaging. *Front. Cardiovasc. Med.* **7**, 119 (2020).
11. R. J. Colchester, C. Little, G. Dwyer, S. Noimark, E. J. Alles, E. Z. Zhang, C. D. Loder, I. P. Parkin, I. Papakonstantinou, P. C. Beard, M. C. Finlay, R. D. Rakhit, A. E. Desjardins, All-optical rotational ultrasound imaging. *Sci. Rep.* **9**, 5576 (2019).
12. Y. Zhang, Y. Liang, L. Jin, B. Guan, 125 μm fiber based all-optical ultrasound probes for pulse-echo imaging. *Chin. Opt. Lett.* **17**, 070604 (2019).
13. S.-L. Chen, L. J. Guo, X. Wang, All-optical photoacoustic microscopy. *Photoacoustics* **3**, 143–150 (2015).
14. M. C. Finlay, C. A. Mosse, R. J. Colchester, S. Noimark, E. Z. Zhang, S. Ourselin, P. C. Beard, R. J. Schilling, I. P. Parkin, I. Papakonstantinou, A. E. Desjardins, Through-needle all-optical ultrasound imaging in vivo: A preclinical swine study. *Light Sci. Appl.* **6**, e17103 (2017).
15. Y. Hou, J.-S. Kim, S.-W. Huang, S. Ashkenazi, L. J. Guo, M. O'Donnell, Characterization of a broadband all-optical ultrasound transducer-from optical and acoustical properties to imaging. *IEEE Trans. Ultrason. Ferroelectr. Freq. Control* **55**, 1867–1877 (2008).
16. C. D. Little, R. J. Colchester, S. Noimark, G. Manmathan, M. C. Finlay, A. E. Desjardins, R. D. Rakhit, Optically generated ultrasound for intracoronary imaging. *Front. Cardiovasc. Med.* **7**, 525530 (2020).
17. Y. Miida, Y. Matsuura, All-optical photoacoustic imaging system using fiber ultrasound probe and hollow optical fiber bundle. *Opt. Express* **21**, 22023–22033 (2013).
18. C. Sheaff, S. Ashkenazi, in *Photons Plus Ultrasound: Imaging and Sensing 2014* (SPIE, 2014), vol. 8943, pp. 687–694.
19. S.-L. Chen, Review of laser-generated ultrasound transmitters and their applications to all-optical ultrasound transducers and imaging. *Appl. Sci.* **7**, 25 (2017).
20. W.-Y. Chang, W. Huang, J. Kim, S. Li, X. Jiang, Candle soot nanoparticles-polydimethylsiloxane composites for laser ultrasound transducers. *Appl. Phys. Lett.* **107**, 161903 (2015).
21. L. Lan, Y. Xia, R. Li, K. Liu, J. Mai, J. A. Medley, S. Obeng-Gyasi, L. K. Han, P. Wang, J.-X. Cheng, A fiber optoacoustic guide with augmented reality for precision breast-conserving surgery. *Light Sci. Appl.* **7**, 2 (2018).
22. S. H. Lee, M.-a. Park, J. J. Yoh, H. Song, E. Y. Jang, Y. H. Kim, S. Kang, Y. S. Yoon, Reduced graphene oxide coated thin aluminum film as an optoacoustic transmitter for high pressure and high frequency ultrasound generation. *Appl. Phys. Lett.* **101**, 241909 (2012).
23. X. Du, J. Li, G. Niu, J.-H. Yuan, K.-H. Xue, M. Xia, W. Pan, X. Yang, B. Zhu, J. Tang, Lead halide perovskite for efficient optoacoustic conversion and application toward high-resolution ultrasound imaging. *Nat. Commun.* **12**, 3348 (2021).
24. M. Seeger, D. Soliman, J. Aguirre, G. Diot, J. Wierzbowski, V. Ntziachristos, Pushing the boundaries of optoacoustic microscopy by total impulse response characterization. *Nat. Commun.* **11**, 2910 (2020).
25. R. K. Poduval, S. Noimark, R. J. Colchester, T. J. Macdonald, I. P. Parkin, A. E. Desjardins, I. Papakonstantinou, Optical fiber ultrasound transmitter with electrospun carbon nanotube-polymer composite. *Appl. Phys. Lett.* **110**, 223701 (2017).
26. S. Noimark, R. J. Colchester, B. J. Blackburn, E. Z. Zhang, E. J. Alles, S. Ourselin, P. C. Beard, I. Papakonstantinou, I. P. Parkin, A. E. Desjardins, Carbon-nanotube–PDMS composite

coatings on optical fibers for all-optical ultrasound imaging. *Adv. Funct. Mater.* **26**, 8390–8396 (2016).
27. H. Won Baac, J. G. Ok, H. J. Park, T. Ling, S.-L. Chen, A. J. Hart, L. J. Guo, Carbon nanotube composite optoacoustic transmitters for strong and high frequency ultrasound generation. *Appl. Phys. Lett.* **97**, 234104 (2010).
28. E. Zhang, J. Laufer, P. Beard, Backward-mode multiwavelength photoacoustic scanner using a planar Fabry–Perot polymer film ultrasound sensor for high-resolution three-dimensional imaging of biological tissues. *Appl. Optics* **47**, 561–577 (2008).
29. S. Ashkenazi, Y. Hou, T. Buma, M. O'Donnell, Optoacoustic imaging using thin polymer étalon. *Appl. Phys. Lett.* **86**, 134102 (2005).
30. J. A. Guggenheim, J. Li, T. J. Allen, R. J. Colchester, S. Noimark, O. Ogunlade, I. P. Parkin, I. Papakonstantinou, A. E. Desjardins, E. Z. Zhang, P. C. Beard, Ultrasensitive plano-concave optical microresonators for ultrasound sensing. *Nat. Photonics* **11**, 714–719 (2017).
31. H. Li, B. Dong, Z. Zhang, H. F. Zhang, C. Sun, A transparent broadband ultrasonic detector based on an optical micro-ring resonator for photoacoustic microscopy. *Sci. Rep.* **4**, 4496 (2014).
32. A. Maxwell, S.-W. Huang, T. Ling, J.-S. Kim, S. Ashkenazi, L. J. Guo, Polymer microring resonators for high-frequency ultrasound detection and imaging. *IEEE J. Sel. Top. Quantum Electron.* **14**, 191–197 (2008).
33. C. Pieters, W. J. Westerveld, H. Mahmud-Ul-Hasan, S. Severi, J. Kjellman, R. Jansen, V. Rochus, X. Rottenberg, in *Photons Plus Ultrasound: Imaging and Sensing 2022* (SPIE, 2022), vol. 11960, pp. 307–317.
34. G. Wissmeyer, D. Soliman, R. Shnaiderman, A. Rosenthal, V. Ntziachristos, All-optical optoacoustic microscope based on wideband pulse interferometry. *Opt. Lett.* **41**, 1953–1956 (2016).
35. L. Riobó, Y. Hazan, F. Veiras, M. Garea, P. Sorichetti, A. Rosenthal, Noise reduction in resonator-based ultrasound sensors by using a CW laser and phase detection. *Opt. Lett.* **44**, 2677–2680 (2019).
36. G. Wissmeyer, R. Shnaiderman, D. Soliman, V. Ntziachristos, in *Photons Plus Ultrasound: Imaging and Sensing 2017* (SPIE, 2017), vol. 10064, pp. 297–303.
37. R. W. Drever, J. L. Hall, F. V. Kowalski, J. Hough, G. Ford, A. Munley, H. Ward, Laser phase and frequency stabilization using an optical resonator. *Appl. Phys. B* **31**, 97–105 (1983).
38. B. E. Treeby, B. T. Cox, k-Wave: MATLAB toolbox for the simulation and reconstruction of photoacoustic wave fields. *J. Biomed. Opt.* **15**, 021314 (2010).
39. G. S. Mintz, S. E. Nissen, W. D. Anderson, S. R. Bailey, R. Erbel, P. J. Fitzgerald, F. J. Pinto, K. Rosenfield, R. J. Siegel, E. M. Tuzcu, American College of Cardiology clinical expert consensus document on standards for acquisition, measurement and reporting of intravascular ultrasound studies (IVUS). A report of the american college of cardiology task force on clinical expert consensus documents. *J. Am. Coll. Cardiol.* **37**, 1478–1492 (2001).
40. H. Lin, D. E. Day, J. O. Stoffer, Optical and mechanical properties of optically transparent poly(methyl methacrylate) composites. *Polym. Eng. Sci.* **32**, 344–350 (1992).
41. E. E. Kiziltas, A. Kiziltas, S. C. Bollin, D. J. Gardner, Preparation and characterization of transparent PMMA–cellulose-based nanocomposites. *Carbohydr. Polym.* **127**, 381–389 (2015).
42. M. Xu, L. V. Wang, Photoacoustic imaging in biomedicine. *Rev. Sci. Instrum.* **77**, 041101 (2006).
43. E. Biagi, F. Margheri, D. Menichelli, Efficient laser-ultrasound generation by using heavily absorbing films as targets. *IEEE Trans. Ultrason. Ferroelectr. Freq. Control* **48**, 1669–1680 (2001).
44. M. Omar, J. Gateau, V. Ntziachristos, Raster-scan optoacoustic mesoscopy in the 25–125 MHz range. *Opt. Lett.* **38**, 2472–2474 (2013).
45. W.-Y. Chang, X. A. Zhang, J. Kim, W. Huang, A. Bagal, C.-H. Chang, T. Fang, H. F. Wu, X. Jiang, Evaluation of photoacoustic transduction efficiency of candle soot nanocomposite transmitters. *IEEE Trans. Nanotechnol.* **17**, 985–993 (2018).
46. T. Lee, L. J. Guo, Highly efficient photoacoustic conversion by facilitated heat transfer in ultrathin metal film sandwiched by polymer layers. *Adv. Opt. Mater.* **5**, 1600421 (2017).
47. G. Wissmeyer, M. A. Pleitez, A. Rosenthal, V. Ntziachristos, Looking at sound: Optoacoustics with all-optical ultrasound detection. *Light Sci. Appl.* **7**, 53 (2018).
48. T. Zhao, L. Su, W. Xia, Optical ultrasound generation and detection for intravascular imaging: A review. *J. Healthc. Eng.* **2018**, 1–14 (2018).
49. T. Berer, I. A. Veres, H. Grün, J. Bauer-Marschallinger, K. Felbermayer, P. Burgholzer, Characterization of broadband fiber optic line detectors for photoacoustic tomography. *J. Biophotonics* **5**, 518–528 (2012).
50. J. Dorighi, S. Krishnaswamy, J. D. Achenbach, Response of an embedded fiber optic ultrasound sensor. *J. Acoust. Soc. Am.* **101**, 257–263 (1997).
51. L. Flax, J. Cole, R. De Paula, J. Bucaro, Acoustically induced birefringence in optical fibers. *J. Opt. Soc. Am.* **72**, 1159–1162 (1982).
52. E. Domingo, J. C. Grignola, R. Aguilar, M. L. Messeguer, A. Roman, Pulmonary arterial wall disease in COPD and interstitial lung diseases candidates for lung transplantation. *Respir. Res.* **18**, 1–9 (2017).
53. A. Rosenthal, D. Razansky, V. Ntziachristos, High-sensitivity compact ultrasonic detector based on a pi-phase-shifted fiber Bragg grating. *Opt. Lett.* **36**, 1833–1835 (2011).

Acknowledgments
Funding: This work was supported by the Special Fund for Research on National Major Research Instruments of China (grant no. 62027824). **Author contributions:** L.W. and P.W. conceived the project and designed the imaging system. L.W. and D.M. performed design and assembly of intravascular probes. L.W., Y.Z., B.Z., and Y.H. performed AO-IVUS imaging experiments. Y.F., Y.G., and P.W. discussed the experimental results and gave suggestions. L.W., Y.Z., and D.M. wrote the manuscript. All authors contributed to the study and critically reviewed the manuscript. **Competing interests:** P.W., L.W., and D.M. are inventors on three patents related to this work filed by Beihang University (no. CN113080871B, published 16 September 2022; no. CN113081043B, published 5 July 2022; and no. CN113080869B, published 5 July 2022) and one patent application filed by Beihang University (no. CN113080870A, filed 9 July 2022). The authors declare that they have no other competing interests. **Data and materials availability:** All data needed to evaluate the conclusions in the paper are present in the paper and/or the Supplementary Materials.

Submitted 27 January 2023
Accepted 5 May 2023
Published 9 June 2023
10.1126/sciadv.adg8600